

See discussions, stats, and author profiles for this publication at: <https://www.researchgate.net/publication/228502570>

Nitrogen-Doped In₂O₃ Thin Film Electrodes for Photocatalytic Water Splitting

ARTICLE *in* THE JOURNAL OF PHYSICAL CHEMISTRY C · OCTOBER 2007

Impact Factor: 4.77 · DOI: 10.1021/jp072831y

CITATIONS

89

READS

115

4 AUTHORS, INCLUDING:



Karla R. Reyes-Gil

Sandia National Laboratories

18 PUBLICATIONS 426 CITATIONS

SEE PROFILE



Daniel Raftery

University of Washington Seattle

181 PUBLICATIONS 4,895 CITATIONS

SEE PROFILE

Article

Nitrogen-Doped InO Thin Film Electrodes for Photocatalytic Water Splitting

Karla R. Reyes-Gil, Enrique A. Reyes-García, and Daniel Raftery

J. Phys. Chem. C, **2007**, 111 (39), 14579-14588 • DOI: 10.1021/jp072831y • Publication Date (Web): 12 September 2007

Downloaded from <http://pubs.acs.org> on March 9, 2009

More About This Article

Additional resources and features associated with this article are available within the HTML version:

- Supporting Information
- Links to the 6 articles that cite this article, as of the time of this article download
- Access to high resolution figures
- Links to articles and content related to this article
- Copyright permission to reproduce figures and/or text from this article

[View the Full Text HTML](#)



ACS Publications
High quality. High impact.

Nitrogen-Doped In₂O₃ Thin Film Electrodes for Photocatalytic Water Splitting

Karla R. Reyes-Gil, Enrique A. Reyes-García, and Daniel Raftery*

Department of Chemistry, Purdue University, West Lafayette, Indiana 47907

Received: April 11, 2007; In Final Form: June 26, 2007

New visible-light photocatalysts were prepared by doping In₂O₃ with nitrogen from ethylenediamine (NH₂(CH₂)₂NH₂) or ammonium chloride (NH₄Cl) as the nitrogen source. Nitrogen-doped In₂O₃ powder prepared from NH₂(CH₂)₂NH₂ shows a rhombic structure and a substitutional N-doping, while the powder prepared from NH₄Cl shows a cubic structure and NH_x in interstitial sites. N-doping extended the light absorption of In₂O₃ to the visible region ($\lambda < \sim 650$ nm), narrowing the band gap from 3.5 eV to approximately 2.0 eV. The photocurrent densities of N-doped In₂O₃ electrodes are at least double those of undoped In₂O₃ and approximately 50 times better than N-doped TiO₂ electrodes in the visible region, although optimization will be needed to deliver high photocurrents. This present work shows that In₂O₃ can be suitably doped to produce a promising photocatalyst with improved photoelectrochemical properties for solar hydrogen conversion applications.

1. Introduction

An increased awareness of environmental issues and limited oil reserves has led to a new focus on the development of clean and renewable energy sources. Solar-driven water splitting (solar hydrogen conversion) represents an almost ideal energy source; however, the discovery of new and more efficient photocatalysts for water splitting is still very challenging. Since the pioneering work by Fujishima and Honda demonstrating that crystalline TiO₂ could split water to produce H₂ and O₂ after UV photoexcitation,¹ wide band gap semiconductor n-type metal oxides have been extensively analyzed for water splitting due to their good stability, nontoxicity, low cost, and catalytic activity. However, the overall efficiency of metal oxide semiconductors is still too low for commercial use due to their poor match to the solar spectrum. Although impressive results have been obtained recently with other metal oxides, specifically WO₃,^{2–4} and Fe₂O₃,^{5,6} TiO₂ has been the most widely studied material in the field of solar hydrogen conversion for more than three decades. Initially, a variety of transition metals (such as V,^{7–10} Fe,^{8,10} Cr,^{8,10–12} and others) were employed to dope titanium dioxide (TM-TiO₂) in order to reduce the band gap and allow it to absorb visible light. However, the photocurrent generated in thin films of these materials has not improved, irrespective of the metal ion used. TM-TiO₂ materials have not yet been shown to be suitable for efficient water splitting reactions due to rapid electron–hole recombination and/or thermal instability.^{7,13–15}

New results using anion doping appears to be very promising for reducing the large band gap of metal oxides.^{16–23} In particular, nitrogen doping has attracted much attention for the development of visible-light photocatalysts. The most widely investigated N-doped materials to date are TiO_{2–x}N_x,^{23–32} in which the optical absorption becomes red-shifted into the visible range ($\lambda > 380$ nm), while the material retains the stability of the host metal oxide. N-doped TiO₂ has displayed efficient photocatalytic oxidation of organic compounds using wave-

lengths up to 550 nm.²³ While there is agreement that N-doping of metal oxides leads to visible-light photoactivity, there are different explanations regarding how N-doping achieves this activity. In particular, two different mechanisms have been proposed which involved either interstitial or substitutional N-doping. The interstitial N-doping is likely to be a NO_x^{33,34} or NH_x²⁸ species, which was attributed to the visible-light response.^{28,33,34} We recently reported a ¹⁵N solid-state NMR (SSNMR) study of N-doped TiO₂ providing further evidence supporting the interstitial N-doping of TiO₂.³⁵ The SSNMR results indicate the formation of various amino functionalities of the type NH_x in interstitial sites, while after calcination at high temperature these nitrogen species oxidize to form nitrate (NO₃[–]).³⁵ However, since the work by Asahi in 2001,²³ several theoretical modeling and experimental studies of N-doped TiO₂ have supported substitutional doping, in which O atoms are partially substituted for N atoms in the metal oxide.^{23,30} Most of the X-ray photoelectron spectroscopy (XPS) investigations observed the N-bonding environment as nitridic (Ti–N) or oxynitridic (Ti–N–O or Ti–O–N). Recently, an electron paramagnetic resonance (EPR) and density functional theory (DFT) study consolidated both mechanisms, indicating that nitrogen species present in N-doped TiO₂ can be present in both substitutional and interstitial sites depending on the synthetic method used.³⁶ Our work also points to the presence of multiple doping species in the material.³⁵

While N-doped TiO₂ is by far the most characterized anion-doped metal oxide, good activity under solar conditions for water splitting has not yet been demonstrated successfully. A few other examples of N-doped metal oxides investigated for water splitting can be found, such as Ta₂O_{5–x}N_x, but their performance is not significantly better than TiO_{2–x}N_x.^{37,38} Another example is WO₃, which has also been doped with nitrogen during the sputtering process to lower the band gap to 2.2 eV, and this material shows distinct promise for further development. However, to date, no spontaneous water splitting has been achieved without the use of co-catalysts.⁴ So far, the most active photocatalysts developed for water splitting are primarily transition metal oxides composed of octahedrally coordinated

* To whom correspondence should be addressed. Phone: (765) 494-6070. E-mail: raftery@purdue.edu.

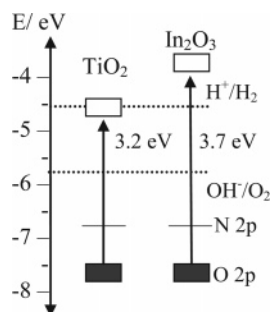


Figure 1. Energy positions (in eV) with respect to the vacuum level for the conduction and valence band edges (white and black rectangles, respectively), of TiO_2 and In_2O_3 .⁵²

d^0 metal ions (Ti^{4+} , Zr^{4+} , Ta^{5+} , and Nb^{5+}).³⁹ Some of the most recent examples of the titanates, zirconates, tantalates, and niobates are M-doped $\text{La}_2\text{Ti}_2\text{O}_7$ ($M = \text{Cr}, \text{Fe}$),⁴⁰ $\text{R}_2\text{Ti}_2\text{O}_7$ and R_3MO_7 ($R = \text{Y}, \text{Yb}, \text{Gd}, \text{La}$; $M = \text{Nb}, \text{Ta}$),^{41,42} and $\text{Sr}_2\text{M}_2\text{O}_7$ ($M = \text{Nb}, \text{Ta}$).⁴³ However, their syntheses require high temperatures to induce the necessary degree of crystallinity, and all have mostly been used in combinations of co-catalysts such as NiO and RuO_2 for the hydrogen evolution.

Recently, the class of materials formally having d^{10} electronic configurations (In^{3+} , Ga^{3+} , Ge^{4+} , Sn^{4+} , and Sb^{5+}) have been investigated in an attempt to develop new photocatalysts for water splitting. The electronic configurations of d^0 and d^{10} are similar in their absence of d electron participation in photoexcitation, which appears to be an important key to their photocatalytic activity.³⁹ Although it would seem that d^{10} indium could potentially form a useful photocatalyst, to date few kinds of In^{3+} -containing photocatalysts have been reported for water splitting including RuO_2 -loaded MIn_2O_4 ($M = \text{Ca}, \text{Sr}, \text{Ba}$), LnInO_3 ($\text{Ln} = \text{La}, \text{Nd}$), and $\text{Sr}_{1-x}\text{M}_x\text{In}_2\text{O}_4$ ($M = \text{Ca}, \text{Ba}$).^{44,45} However, the activities of the aforementioned indates are usually low under visible-light irradiation. In_2O_3 has an excellent conductivity and stability in aqueous systems, and its interfacial band edges are likely positioned to drive the necessary redox reactions, which is an important requirement for photoelectrochemical cells.⁴⁶ An important drawback for the potential use of In_2O_3 for water splitting under solar illumination is its large band gap (3.7 eV), and consequently, In_2O_3 has not been extensively studied for water splitting. There is only a single recent report of $\text{In}(\text{OH})_3\text{S}_2$,⁴⁷ and its photoelectrochemical properties have not been measured. The other reported approach for reducing the band gap of In_2O_3 has been to synthesize compound semiconductor systems, and only a few examples have been reported for water splitting, including $(\text{In}_2\text{O}_3/\text{ZnO})_m$,⁴⁸ $\text{TiO}_2/\text{In}_2\text{O}_3$,⁴⁹ $\text{In}_2\text{O}_3/\text{In}_2\text{S}_3$,⁵⁰ and Cr-doped $\text{Ba}_2\text{In}_2\text{O}_5/\text{In}_2\text{O}_3$.⁵¹ The use of sacrificial reagents has been required in all these cases.

In the present paper, we report the synthesis, characterization, and photoelectrochemical analysis of N-doped In_2O_3 nanoparticles, a novel photocatalyst for water splitting. To our knowledge, In_2O_3 has not been doped with N before. Our approach to doping In_2O_3 with nitrogen in order to reduce its wide band gap is based on the consideration that the d^0 (TiO_2) and d^{10} (In_2O_3) metal oxides have similar electronic configurations and band structures. Our hypothesis is that the N-doping mechanism, in which O 2p orbitals are mixed with N 2p orbitals, is similar in TiO_2 and In_2O_3 due to the fact that both valence bands are formed by the oxygen 2p orbitals, and there is no involvement of the d electrons in the photoexcitation process (see Figure 1).^{44,52} Characterization results described below support this hypothesis in showing that N-doping effectively increases the

visible absorption of In_2O_3 thin film electrodes in a similar fashion to TiO_2 electrodes. In addition, XPS results suggest that the N anions have been incorporated into the In_2O_3 lattice by different doping mechanisms (substitutional and interstitial) depending on the nitrogen source used. In the photoelectrochemical analyses, the N-doped In_2O_3 electrodes were compared with undoped In_2O_3 as well as N-doped TiO_2 , and showed better photocurrent densities under UV–visible and visible irradiation without any co-catalysts or promoters.

2. Experimental Methods

2.1. Synthesis. Indium oxide nanoparticles were fabricated by a sol–gel route based on solvothermal reactions using ethylenediamine (en) [$\text{NH}_2(\text{CH}_2)_2\text{NH}_2$] (Aldrich) or ammonium chloride (am) [NH_4Cl] (Alfa Aesar) to form N-doped In_2O_3 . InCl_3 (1.0 g) (Strem) and deionized water (2 mL) were mixed in a Teflon-lined stainless steel autoclave of 250 mL capacity. After InCl_3 had dissolved, the N-source solution was then transferred into the autoclave and stirred rapidly. NH_4Cl was dissolved in ethanol (20 mL) to form a solution. The autoclave was heated at 190 °C for 24 h. The white precipitate was then filtered and washed with ethanol and water. Finally, the powders were dried and calcinated in air at 500 °C for a period of 2 h (heating rate = 2 °C/min). For the synthesis of undoped In_2O_3 , the intermediates $\text{In}(\text{OH})_3$ and InOOH have been identified previously.⁵³ The hydrolysis reaction of In^{3+} carried out in this solvothermal system formed $\text{In}(\text{OH})_3$. Due to its thermal instability, $\text{In}(\text{OH})_3$ further decomposed to form InOOH , a white precipitate. For the N-doped In_2O_3 , the powder's color changed to bright yellow after calcination.

N-doped TiO_2 powders used for comparison were synthesized in our lab, and the details of this synthesis have been described in our previous work.⁵⁴ Briefly, 30 mL, 0.100 mol, of $\text{Ti}(\text{O}^i\text{Pr})_4$ in isopropyl alcohol (95:5) solution was added dropwise to 50 mL of 28 wt % $\text{NH}_3(\text{l})$ (Lancaster) in 300 mL of deionized water. The white precipitate was stirred for 15 min and acidified by the addition of 2 mL of 70% HNO_3 and heated for 18 h at 80 °C. The sol obtained was allowed to age in loosely capped containers until all the solvents evaporated. Calcination of the synthesized powder was carried out in air for a period of 1 h at 425 °C (heating rate = 2 °C/min).

2.2. Thin Film Electrodes. P25 TiO_2 and In_2O_3 commercial powders (both from Alfa Aesar) were used as controls. All thin film electrodes were prepared following the same general procedure.⁵⁴ A 0.04 g sample of the powders was dispersed in 1 mL of deionized water ultrasonically to form an aqueous sol. A 0.5 mL volume of acetylacetone and 2 drops of Triton (surfactant source) were added to the sol to enhance the final film porosity and facilitate the film's spreadability over glass. Although the particles were not stable for a long period in aqueous basic solution, they could be stabilized in the form of an aqueous sol sufficiently to allow the film preparation. The thin film electrodes were prepared on conductive fluorine tin oxide (FTO) glass by doctor-blading techniques.⁵⁵ The cleaned FTO glass (water, methanol, and acetone ultrasonic bath) was covered on two parallel edges with adhesive tape to control the thickness of the film and to provide a noncoated area for electrical contact. The aqueous sol was applied to the center section of FTO and distributed with a glass rod. After each coating, the films were dried at 60 °C in air for 10 min. The electrodes were coated three times in order to increase the film thickness. Finally, the films were calcined at 500 °C for 2 h in air. The electrical contact was made on one of the noncoated edges. A copper wire was attached to the FTO using silver

epoxy, and the metallic contact was then covered with epoxy resin to isolate it from the electrolyte solution. A glass rod was attached to the back of the conductive glass using epoxy resin for positioning purposes in the photoelectrochemical cell. The thin film electrodes were resistant and stable against corrosion in the electrolyte solution during the whole photoelectrochemical analysis.

2.3. Characterization. X-ray diffraction (XRD), IR, and XPS analyses were performed on the powders after the calcination process. XRD analysis was performed under Cu K α radiation, and the crystalline size was calculated from X-ray line broadening using the Scherer equation. IR spectra were collected using a Perkin-Elmer FT-IR spectrometer. The powder samples were combined with Nujol (paraffin oil) to make a mull and sandwiched between zinc selenide plates before being placed in the spectrometer. XPS survey and high-resolution scans were collected with a Kratos Axis ULTRA X-ray photoelectron spectrometer, and CASAXPS software was used to analyze the XPS data.⁵⁶ UV–visible absorption spectroscopy was performed on the films using a Cary 300 UV–vis spectrophotometer. Assuming the materials are indirect semiconductors, as is the case for N-doped TiO₂, a plot of the modified Kubelka–Munk function $[F(R)E]^{1/2}$ vs the energy of absorbed light E should yield a straight line and the band gap energy can be determined from the intercept.⁵⁷ The film thickness and morphology were determined using cross-sectional and surface scanning electron microscopy (SEM) images, respectively. All imaging was done using an FEI NOVA nanoSEM field emission SEM. Surface images were acquired using the TLD (through-the-lens) detector at 7–8 kV, a 3.5–3.9 working distance, and magnifications of 1–100K when viewed at 30 \times 26 cm. All samples were coated with Pt prior to imaging the surface at high vacuum. The glass was fractured and mounted in a vice holder for cross-sectional viewing to determine thicknesses.

2.4. Photoelectrochemical Measurements. A three electrode potentiostat system was used to measure the photoelectron current, which allowed the measurement of the e[−] and h⁺ pair formation as a function of the externally applied potential necessary for water splitting. The photoelectrodes were placed in the electrolyte (1.0 M KOH), while potentiostatic control was maintained with a Bioanalytical Systems CV-27 potentiostat. Platinum foil was used as the counter electrode and Ag/AgCl as the reference electrode. The illumination source employed was a 300 W Xe arc lamp directed at the quartz photoelectrochemical cell with an intensity of 0.13 W/cm² simulating the reported total solar irradiance of 0.1366 W/cm².⁵⁸ The intensity of the lamp was measured using a photodiode detector (OPHIR Model PD300). A water filter was used to remove the IR energy and avoid overheating. A 1 cm² region of the photoelectrode surface was illuminated with intermittent light exposure. The photocurrent densities were calculated using the difference between the light-off (dark current) and light-on currents acquired consecutively.

3. Results and Discussion

3.1. XRD. Peaks in the XRD spectra for the N-doped In₂O₃ powders (Figure 2a,b) show a considerable broadening relative to those for undoped In₂O₃ powder (Figure 2c). The average crystal size calculated using the Scherer equation for N-doped In₂O₃ powders synthesized from am and en is 18 and 19 nm, respectively and is 27 nm for undoped In₂O₃ powders. The XRD patterns for P25 TiO₂ powder and N-doped TiO₂ powder are shown in Figure 2d and Figure 2e, respectively. The average crystal sizes are 30 and 20 nm for the P25 TiO₂ and N-doped

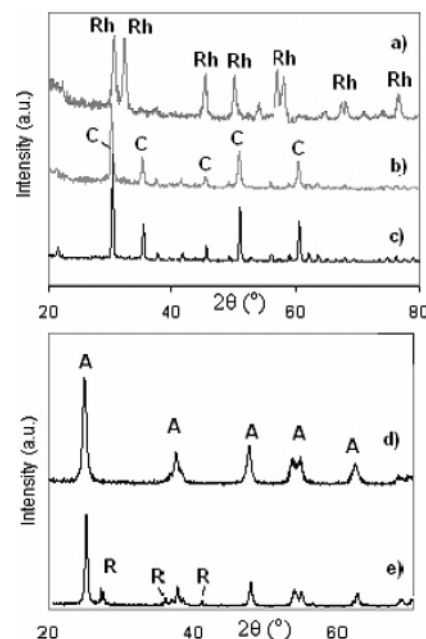


Figure 2. XRD patterns for (a) (en) N-doped In₂O₃, (b) (am) N-doped In₂O₃, (c) undoped In₂O₃ powders, (d) N-doped TiO₂, and (e) undoped TiO₂ electrodes. The label “C” denotes cubic phase and “Rh” the rhombohedral phase of In₂O₃. The label “A” denotes anatase phase and “R” the rutile phase of TiO₂.

TiO₂ powders, respectively. The peak broadening observed as a consequence of N-doping has been previously reported.⁵⁹ Only a small variation in intensity was observed, indicating that the crystallinity and the film thickness are similar for all the doped and undoped films.⁶⁰

Indium oxide has two crystalline structures: the cubic bixbyite-type structure, and the rhombohedral or corundum structure. Under normal conditions In₂O₃ crystallizes in the cubic form, even when it has been prepared by different methods: calcination, laser ablation, or spray pyrolysis. The rhombohedral structure is a high-pressure phase and consequently has been rarely produced. In both structures the cations are 6-coordinated and the anions are 4-coordinated, the cation–anion distances are nearly identical, and the densities are similar.⁶¹ However, the rhombic phase exhibits better physical properties than the cubic phase, such as a more stable conductivity, that result from a better packing of the anion layers.⁶² XRD analysis shows that N-doped In₂O₃ powder synthesized from NH₄Cl and the In₂O₃ commercial powder have a well-defined cubic structure. The powders are finely polycrystalline and are highly oriented along (222) at $2\theta = 30.56^\circ$, with a single phase of In₂O₃. However, the samples prepared with en show a rhombic phase. InN characteristic peaks are not observed in any of the N-doped In₂O₃. The XRD patterns of the N-doped TiO₂ powder displayed well-defined TiO₂ anatase phase and no evidence of TiN was found.⁵⁴ This result is in good agreement with most N-doped TiO₂ studies, where at low doping levels no sign of TiN or any other peaks other than those of TiO₂ were observed.⁶⁰ All the N-doped materials preserve the crystal structure of the host materials (TiO₂ or In₂O₃). With N-doping in interstitial or even substitutional sites, the desired crystal phase integrity of the host material is expected to be conserved due to the small change in ion size from O to N that limits the disturbance in the crystal lattice. However, at high dopant concentrations, the perturbation or destruction of the host lattice could occur, potentially decreasing the photocatalytic activity.⁶³

3.2. IR. Paraffin oil was used as a mulling agent because it is chemically inert and has a relatively uncomplicated IR

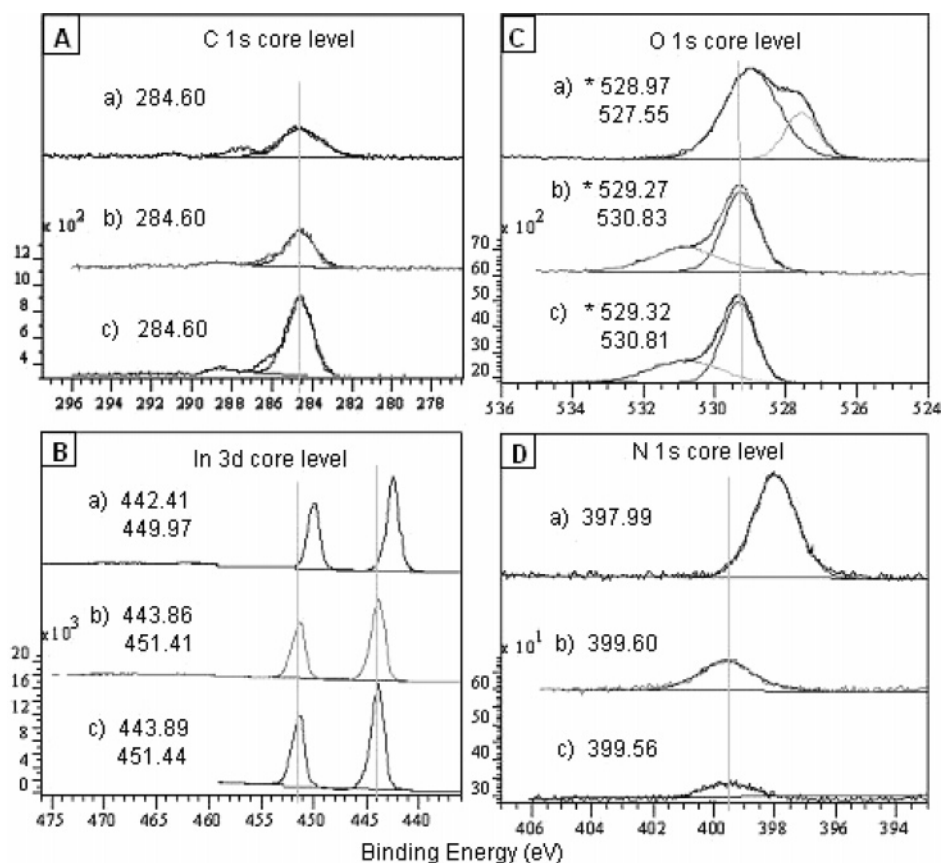


Figure 3. XPS high-resolution spectra of (A) C 1s, (B) In 3d, (C) O 1s, and (D) N 1s core levels for (a) (en) N-doped In_2O_3 , (b) (am) N-doped In_2O_3 , and (c) In_2O_3 commercial powders. Intensity scales for (a) and (b) data are the same as for (c) in each figure, but are offset for ease of visualization.

TABLE 1: Binding Energies and Atomic Ratios for In, O, and N in N-Doped In_2O_3 and In_2O_3 Powders and for Ti, O, and N in N-Doped TiO_2

powder	In 3d _{5/2}		O 1s		N 1s	
	BE (eV)	atom % ^a	BE (eV)	atom % ^a	BE (eV)	atom % ^a
(a) (en) N-doped In_2O_3	442.4	43.2	529.0	50.2	398.0	6.5
(b) (am) N-doped In_2O_3	443.9	45.6	529.3	50.4	399.6	4.0
(c) In_2O_3 commercial	443.9	47.2	529.3	51.9	399.6	1.0

powder	Ti 2p _{3/2}		O 1s		N 1s	
	BE (eV)	atom % ^a	BE (eV)	atom % ^a	BE (eV)	atom % ^a
(d) N-doped TiO_2	458.7	31.8	529.7	65.8	399.4, 406.6	2.4

^a The atomic percent (atom %) of each element was determined using XPS high-resolution data and normalization by the following sensitivity factors (RSF): 13.32 for In 3d_{5/2}, 2.93 for O 1s, 1.80 for N 1s, and 5.22 for Ti 2p_{3/2}.

spectrum, with major peaks at 2950–2800, 1465–1450, and 1380–1370 cm^{-1} . The spectra for the three In_2O_3 powders (undoped commercial In_2O_3 , (en) N-doped In_2O_3 , and (am) N-doped In_2O_3) do not show the presence of any major peaks besides those of paraffin oil. The IR results thus indicate a lack of any organic residues from the initial reagents or solvents, as would be expected given the high temperatures used in the calcination process (500 °C). The IR spectra are presented as Supporting Information Figure S1.

3.3. XPS. **3.3.1. Atomic Ratios.** We have examined three areas of the XPS spectrum: the In 3d region (440–450 eV, Figure 3B), the O 1s region (525–535 eV, Figure 3C), and the N 1s region (395–405 eV, Figure 3D). The positions and atomic ratios of In, O, and N are summarized in Table 1. The atomic ratios were determined using the XPS high-resolution peaks, taking into account the sensitivity factor (RSF) for each element. The N atomic ratio was 1.0%, 4.0%, and 6.5% for In_2O_3

commercial, (am) N-doped In_2O_3 , and (en) N-doped In_2O_3 powder, respectively. The N presence found in the undoped In_2O_3 sample is attributed to superficial environmental contamination, as has been reported previously for undoped TiO_2 films.²³ The nitrogen excess of the doped materials comes from the precursor reagents (am and en). The N-doped TiO_2 powder was also analyzed by XPS (Figure 4) and was found to contain 2.4% N.

3.3.2. C 1s Core Level. The survey spectra of all the In_2O_3 powders confirmed the presence of In, O, N, and C. The binding energies (BEs) were calibrated using the C 1s energy of 284.6 eV. As shown in Figure 3, a single C 1s peak was observed in all three spectra and attributed to adventitious carbon that seems to exhibit an unavoidable presence on all air-exposed materials. This result is in good agreement with the IR spectra and supports the absence of carbon impurities resulting from the organic reagents and solvents used in the synthesis.

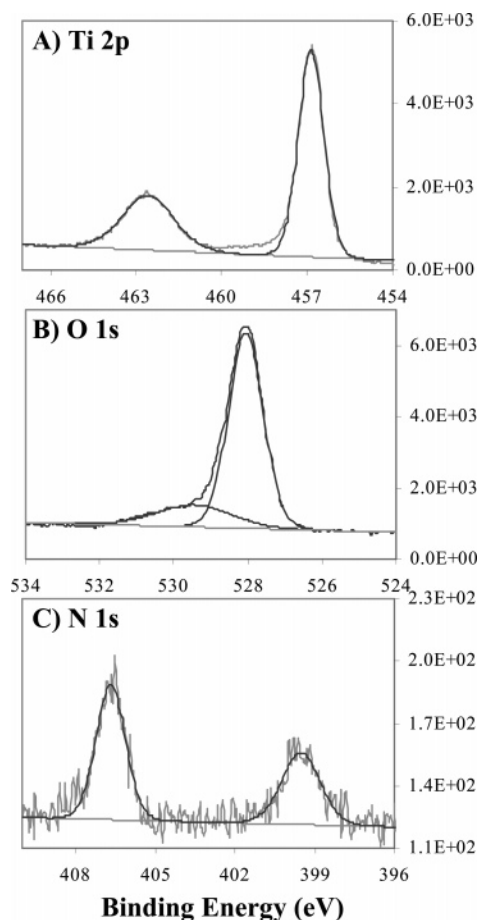


Figure 4. XPS high-resolution spectra of (A) Ti 2p, (B) O 1s, and (C) N 1s core levels for N-doped TiO₂ powder.

3.3.3. In 3d/Ti 2p Core Level. As shown in Figure 3B, the In 3d_{5/2} peak for the commercial In₂O₃ and (am) N-doped In₂O₃ appears at 443.9 eV, very similar to the value reported in the literature (443.8 eV).^{64,65} However, the (en) N-doped In₂O₃ sample shows a shift to lower BE (442.4 eV), close to the region reported for InN.⁶⁵ The creation of InN as secondary product of our synthesis is ruled out due to the presence of the single In 3d_{5/2} peak, which, according to the XRD data, was identified as In₂O₃ in the rhombohedral phase. Instead, this BE shift suggests a reduction of the In cation valence state due to a substitutional doping. When N replaces O, the valence state of In³⁺ is reduced to In²⁺, causing the BE of the In 3d_{5/2} peak to shift to lower energy. This situation has been seen, for instance, in the In bonding to oxygen in In₂O₃ that results in a higher BE than In bonding to nitrogen in InN.⁶⁶ This is also consistent for TiO₂ and substitutional N-doped TiO₂, in which the lower BE of the Ti 2p_{3/2} peak after nitrogen treatment can be attributed to nitrogen substitutional doping.^{29,67} Sathish et al. explained that this lower BE shift suggests that N-substitution modifies the electronic interaction of Ti with the oxygen anions.⁶⁷ As N is less electronegative than O, the electron density around the

anions decreases, increasing the electron density around the cations.⁶⁷ For the N-doped TiO₂ synthesized in our lab, the Ti 2p_{3/2} peak at 458.5 eV was found (Figure 4A), in good agreement with the value reported in the literature for TiO₂.²⁸ No BE shift in the Ti peak was observed, indicating an interstitial doping for this material.

3.3.4. O 1s Core Level. Figure 3C shows that the O 1s core level is composed of at least two components. The peak positions and intensities are reliably determined by a standard curve fitting procedure using CASAXPS software.⁵⁶ The O 1s signal at 529.3 eV is assigned to In₂O₃ according to the literature,⁶⁴ while the signal at 530.8 eV is probably due to oxygen in surface hydroxyl groups.⁶⁸ (en) N-doped In₂O₃ samples show a shift to lower energy (529.0 eV) for the O 1s peak that is assigned to In₂O₃. This shift is similar to results found for substitutional N-doped TiO₂ samples, in which the P25 TiO₂ sample shows an O 1s peak at 530.8 eV, versus a shift to 530.0 eV that is observed for the nitrogen-doped TiO₂ samples.²⁹ As can be seen in Figure 3C-a, an additional peak at 527.55 eV was observed for the (en) N-doped In₂O₃ samples. An O 1s peak at such a low binding energy has also been observed for B/F co-doped TiO₂, but remains unassigned.⁶⁹ For the N-doped TiO₂ synthesized in our lab, two components were identified (Figure 4B). The signals at 529.7 and 531.1 eV are assigned to TiO₂ and hydroxyl groups, respectively.

3.3.5. N 1s Core Level. The XPS high-resolution spectra of N 1s show one peak at 399.6 eV and another at 398.0 eV for (am) N-doped In₂O₃ and (en) N-doped In₂O₃ powder, respectively (see Figure 3D). The difference of 1.6 eV between these two N 1s peaks correlates with the theoretical calculations of the relative values for the N 1s state in substitutional versus interstitial sites with a higher core level BE for the interstitial site.³⁶ These calculations also compare well with the experimentally observed peaks for N-doped TiO₂, one at ~397 eV (attributed to substitutional N) and the other at >399 eV (interstitial N). In light of this correlation and the XPS spectra of In 3d and O 1s core levels discussed previously, we can attribute the peaks at 398.0 and 399.6 eV to substitutional and interstitial doping, respectively.

To determine the N species present in the N-doped In₂O₃ powders, the BEs for N species in different environments are summarized in Table 2. Both peaks appear at higher BEs than the typical energy for InN (397 eV)⁶⁶ and at lower BEs than free or adsorbed N species on metal oxides. The N 1s peak at 399.6 eV for (am) N-doped In₂O₃ can be attributed to NH_x located in interstitial sites due to the excellent match with a previous study.²⁸ The possibility of NO in interstitial sites as reported for Sato et al.⁷⁰ could not be ruled out due to the proximity of these two experimental values (399.6 and 400 eV), although highly oxidized N species such as NO₂ and NO₃ (405 and 408 eV, respectively⁷¹) are improbable. For (en) N-doped In₂O₃, the peak at 398.0 eV corresponds to N species significantly more reduced than those of (am) N-doped In₂O₃, diminishing the possibility of NH_x or NO_x species being present and suggesting the presence of the N anion. The identification

TABLE 2: Binding Energies (in eV) for N Species in Selected Metal Oxide Environments

BE (eV) of adsorbed N species on metal oxides				BE (eV) of N species in N-doped TiO ₂			
adsorbed amines on TiO ₂ ⁷⁷		adsorbed NO _x on ZnO ⁷¹		interstitial		substitutional	
NH ₃	400.1	NO	400–402	NH _x ²⁸	399.6	Ti–N bond ^{23,36}	396–397
CH ₃ CH ₂ NH ₂	400.6	NO ₂	404–405	NO ⁷⁰	400	N [–] in O–Ti–N ⁶⁷	398.2
CH ₃ –NH ₂ ⁺ –CH ₃	401.1	NO ₃	407–408			Ti–O–N ²⁹	400.7
						Ti–N–O ^{59,78}	401.3

of substitutional N species based only on the XPS results has been very controversial.^{67,72,73} For substitutional N-doped TiO₂ materials, a peak around 397 eV has been detected and attributed to a Ti–N bond by several authors;^{23,24,31} however, that peak is not always observed. Burda et al. attributed the signals at higher BEs (401.3²⁹ and 400.7 eV⁵⁹) to “a minimal structure fragment within the TiO₂ lattice in which nitrogen is likely connected in some manner to Ti, and, as well to other atoms (Ti or O) to complete its valency.”⁷² Sathish et al. reported a single peak at 398.2 eV, which was attributed to the anionic N[−] in O–Ti–N linkages.⁶⁷ The authors explained that this value is a little higher than the BE of TiN (~397 eV) because the electron density on nitrogen is reduced for the oxygen in the TiO₂ lattice. However, they ruled out the possibility of a direct interaction of N and O in the lattice (Ti–O–N and/or Ti–N–O linkages), because this might cause a significant BE increment of the N 1s peak (>400 eV). The discrepancies in the XPS findings of N-doped TiO₂ materials could be due to differences in preparation procedures that largely affect nitrogen XPS spectral features.³⁶ Our synthetic method is similar to that of Sathish et al. in the choice of the metal precursors (TiCl₃ and InCl₃) and the temperature range of calcination in air (400–500 °C). Also, our XPS results for (en) N-doped In₂O₃ sample show similar lower BE shifts for the metal cation and the single N 1s peak at 398.0 eV, which are very close to Sathish’s result of 398.2 eV for N-doped TiO₂. Based on these XPS results, we believe the peak at 398.0 eV can be assigned to anionic N[−] in O–In–N linkages.

For the N-doped TiO₂ synthesized in our lab, two N peaks were found at 406.6 and 399.4 eV (Figure 4C). According to the BE reported (Table 2), the bigger peak at 406.6 eV is assigned to NO₃ and the smaller peak at 399.4 eV to NH_x in interstitial sites. In a previous article, we reported a ¹⁵N SSNMR study of N-doped TiO₂, as synthesized in this work.³⁵ The SSNMR results indicate the formation of various amino functionalities of the type NH_x in interstitial sites, while after calcination at high temperature (>550 °C) these nitrogen species oxidize to form nitrate (NO₃[−]).³⁵ At 500 °C, the temperature used in this work, both N species (NH_x and NO₃[−]) were detected using SSNMR, with NO₃[−] being predominant.³⁵ The XPS results of the present work are in good agreement with our previous SSNMR study, providing further evidence to support the interstitial N-doping of TiO₂.

In summary, the XPS spectra show that samples prepared using en show low BEs for the In 3d_{5/2} and O 1s peaks compared to those in undoped In₂O₃, indicating that N atoms are perturbing the lattice. Comparing our data with N-doped TiO₂ data reported in the literature, we can conclude that the shifts to low BEs for (en) N-doped In₂O₃ powder are probably due to a substitutional doping. The high-resolution spectra of N 1s show a peak at 398.0 eV for the samples prepared using en, probably due to a nonstoichiometric O–In–N arrangement. For the samples prepared using NH₄Cl, no corresponding shifts are observed in In and O peaks, but the presence of an N 1s peak at 399.6 eV indicates that N species (probably NH_x species) are in the interstitial spaces. In light of these XPS findings, we suggest that N anions have been incorporated into the lattice of In₂O₃ nanoparticles in different ways (substitutional and interstitial), depending on the N source used.

The important role played by the different N sources could be explained by the chemical properties of each N-containing reagent and how these properties affect the hydrolysis of In³⁺. Ethylenediamine is a chelating agent and strongly combines with water to form hydrogen bonds. It also likely coordinates with

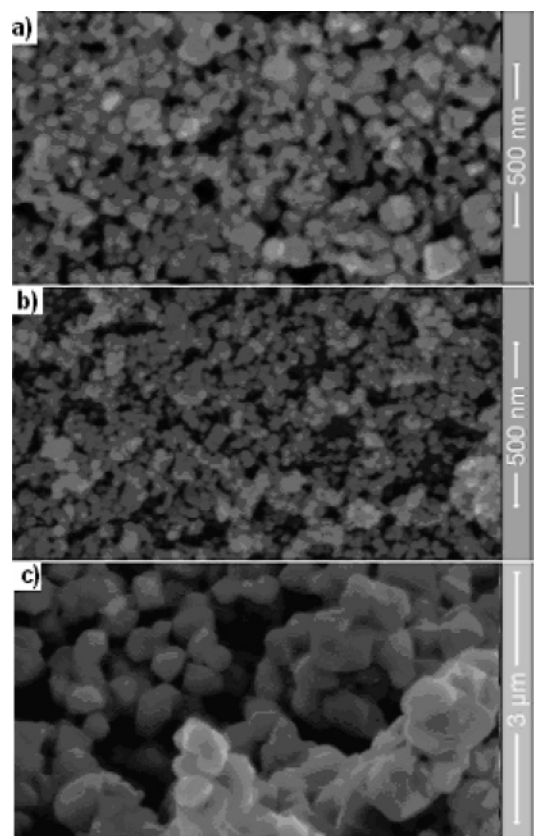


Figure 5. SEM surface images of thin films made from (a) (en) N-doped In₂O₃, (b) (am) N-doped In₂O₃, and (c) In₂O₃ commercial powders.

In³⁺ to form an ethylenediamine–ion complex.⁵³ Thus, the hydrolysis rate of In³⁺ to form In₂O₃ is decreased considerably such that a reaction between indium and nitrogen can become possible. On the other hand, NH₄Cl is a water-soluble salt without any chelating properties. The hydrolysis of In³⁺ to form In₂O₃ is highly favorable and much faster than any reaction between indium and nitrogen. Lacking the association provided by the chelating agent, the formation of In₂O₃ is not impeded by NH₄Cl. After the formation of In₂O₃, the NH_x are probably localized in interstitial sites.

3.4. SEM. To evaluate the spectroscopic and photoelectrochemical properties of N-doped In₂O₃ materials, thin film electrodes were made from the synthesized doped powders and from commercial powders (P25 TiO₂ and In₂O₃) used as controls. As shown in Figure 5, the thin film prepared from either (en) (Figure 5a) or (am) (Figure 5b) N-doped In₂O₃ powders appears to have more tightly aggregated small crystals in a fairly confluent coating than the thin films prepared from In₂O₃ commercial powder (Figure 5c). The cross-sectional images showed varied thicknesses from about 0.5 to 1.5 μm with a 1.0 μm average. The powder agglomeration and the resolution do not permit a quantitative determination of the crystal size, but SEM evidence indicating the larger size for the commercial powder is in agreement with the XRD patterns.

3.5. UV–Visible Absorption Spectra. All the UV–visible spectra for N-doped In₂O₃ thin films show that the incorporation of N into the In₂O₃ host matrix clearly leads to a red shift in the optical response and a concomitant reduction of the band gap energy, as shown in Figure 6A. The absorption onset of (am) N-doped In₂O₃ and (en) N-doped In₂O₃ electrodes is 690 and 600 nm, respectively, compared to 380 nm for the undoped In₂O₃ electrodes. The band gaps determined from the Kubelka–

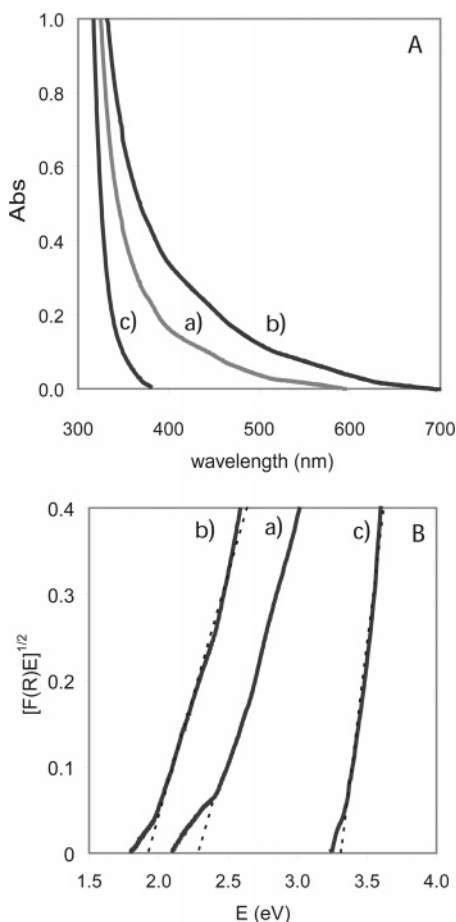


Figure 6. (A) UV-vis spectra and (B) transformed diffuse reflectance spectra for (a) (en) N-doped In_2O_3 , (b) (am) N-doped In_2O_3 , and (c) undoped In_2O_3 thin film electrodes.

Munk function⁵⁷ show a significant narrowing for the N-doped In_2O_3 compared to the undoped In_2O_3 (Figure 6B). The band gap of (am) N-doped In_2O_3 is in the range of 1.9–2.1 eV, and for (en) N-doped In_2O_3 it is in the range of 2.4–2.7 eV, while the band gap of undoped In_2O_3 is around 3.5 eV. The UV-visible spectrum for our N-doped TiO_2 sample was reported previously, showing an absorption maximum centered at 435 nm and the absorption onset at about 550 nm.³⁵

These observed red shifts in absorption and the band gap narrowing can be attributed to N-doping, but how N atoms change the band structure of the metal oxide host is still quite controversial. Asahi and co-workers claim that the visible-light sensitivity of N-doped TiO_2 is due to the narrowing of the band gap by mixing the N 2p and O 2p states.²³ Irie and co-workers suggest that an isolated and narrow energy band formed above the valence band is responsible for the visible-light response rather than a narrowing of the band gap.²⁴ Other authors disagree about the role of substitutional doping and attribute the beneficial doping effect to NO_x impurities³³ or NH_x located in an interstitial site in the TiO_2 lattice.²⁸ Di Valentin and co-workers computed the electronic band structures for both N-doped model systems (substitutional and interstitial doping sites) that could form localized states in the band gap.³⁶ They found that substitutional N states lie just above the valence band, while interstitial N states lie higher in the band gap region. Excitation from these occupied high-energy states to the conduction band can account for the optical absorption edge shift toward the visible region.³⁶ Our experimental results are in good agreement with those of the Di Valentin study, as we observe a larger shift toward the visible region for (am) N-doped In_2O_3 electrodes, which we

attribute to an interstitial doping. However, we see little to no evidence of a distinct interband state from the UV-vis data. Our previous work on N-doped TiO_2 indicates that such materials may be complicated by the presence of several types of N-dopants and sites.³⁵

3.6. Photoelectrochemical Measurements. In addition to a changed optical response, the photoelectrochemical analysis shows that N-doped In_2O_3 materials have favorable photoactivity without sacrificial reagents or co-catalysts. N-doped In_2O_3 thin film electrodes were compared with electrodes made from In_2O_3 commercial particles, P25 TiO_2 powder, and N-doped TiO_2 powder. The results of the photoelectrochemical experiments acquired as a function of applied potential using 1.0 M KOH as the electrolyte and irradiated using UV-vis light are summarized in Figure 7A. The photocurrent densities for the N-doped In_2O_3 electrodes obtained were at least triple those for the undoped In_2O_3 electrodes with equivalent film thickness ($\sim 1 \mu\text{m}$ according to the SEM images). All dark currents were below $10 \mu\text{A}$. As the experimental conditions (electrolyte solution, room temperature, and UV-vis light intensity) were kept constant, the enhancement of the photoactivity can be attributed to nitrogen doping. As shown in Figure 7A, the (en) N-doped In_2O_3 photoelectrodes show better photoactivity under UV-vis, indicating that the substitutional doping results in a better photocurrent than interstitial doping without sacrificial reagents.

In addition, the photocurrents for the N-doped In_2O_3 electrodes are higher than those for the N-doped TiO_2 electrodes by a factor of more than 10 under UV-vis irradiation. Part of this enhancement is due to the hosts' properties. Although TiO_2 has a lower band gap, undoped In_2O_3 electrodes show better photocurrent density than undoped TiO_2 electrodes. This unexpected result is in good agreement with the study by Pozanyak et al. regarding the structural, optical, and photoelectrochemical properties of TiO_2 versus In_2O_3 .⁴⁹ The electrical conductivity measurements showed that In_2O_3 particles have better conductivity and a significantly lower intrinsic resistivity than TiO_2 . This good conductivity helps to preserve the separation of electrons and holes, reducing the recombination losses and improving the photocurrents of In_2O_3 electrodes. Another fact is that the N concentration in doped In_2O_3 materials is higher than in doped TiO_2 according to the XPS results (Table 1), although all the samples are considered highly doped ($> 2\%$ N). More studies are needed to determine how the dopant concentration affects the photoelectrochemical properties. Previous work has reported that high N concentrations in TiO_2 materials reduce their photoactivity.⁶³

To verify that N-doping increases the efficiency under visible illumination, a 378 nm cutoff filter was used to remove the UV light. Figure 7B shows that the photocurrent densities of N-doped In_2O_3 electrodes are double those for undoped In_2O_3 , although they are reduced significantly compared to the UV-vis irradiation. While N-doped In_2O_3 appears to be about 50 times better than N-doped TiO_2 under visible-light irradiation, the N-doping effect in In_2O_3 and TiO_2 hosts is relatively similar, resulting in a doubling of the photocurrents compared to the respective undoped hosts.

In addition to increasing the visible-light absorption, another important step in achieving the goal of improved photoactivity is to avoid e^-/h^+ recombination, which reduces the efficiency of the surface photochemistry.⁷⁴ The addition of sacrificial reagents, such as methanol, to the electrolyte has been used in the past to reduce the e^-/h^+ recombination rate.⁷⁵ The effect of methanol addition to the electrolyte was investigated by varying

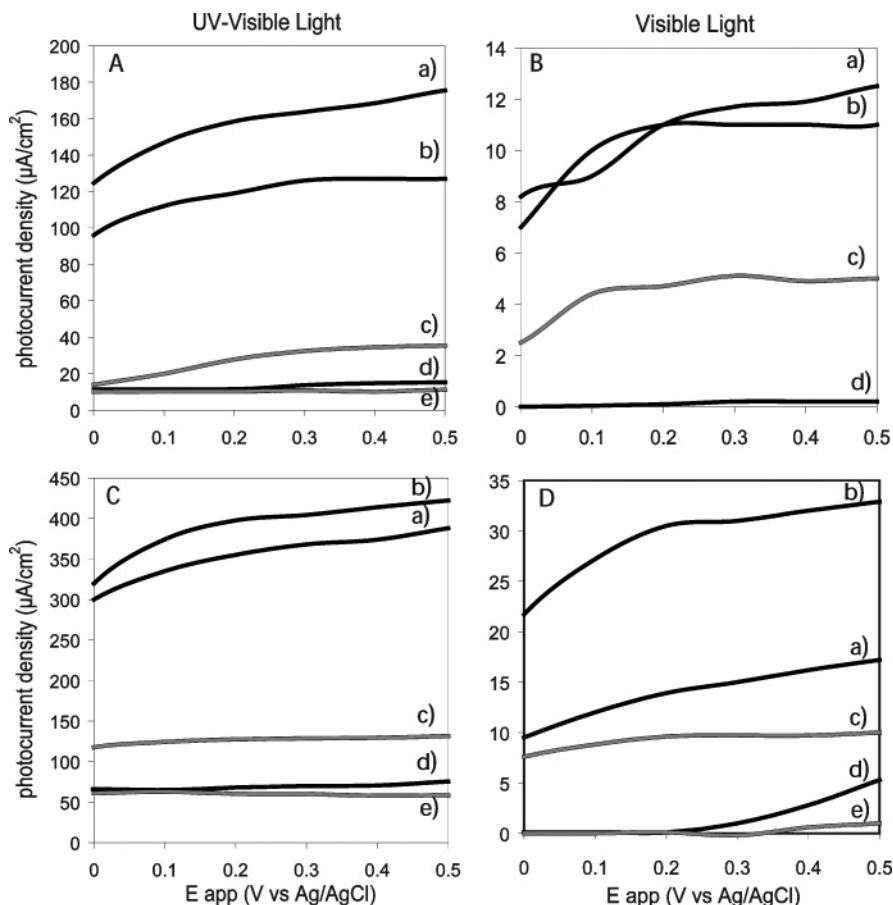


Figure 7. Photocurrent densities for (a) (en) N-doped In₂O₃, (b) (am) N-doped In₂O₃, (c) undoped In₂O₃, (d) N-doped TiO₂, and (e) undoped TiO₂ electrodes. The electrodes were suspended in a 1.0 M KOH solution (A, B) and illuminated with 130 mW/cm² UV/visible (A) and visible light ($\lambda > 378$ nm) (B). The photocurrent density for (e) undoped TiO₂ electrodes under visible light (B) was negligible. CH₃OH was then added to the KOH solution (C, D), and the experiments were repeated with 130 mW/cm² UV/visible (C) and visible light ($\lambda > 378$ nm) (D).

the concentration of methanol in KOH for the different In₂O₃ and TiO₂ electrodes; the best photoelectrochemical performance was obtained using 20% CH₃OH and 80% KOH (v/v). In experiments involving KOH as the electrolyte with added CH₃OH, this ratio was kept constant in order to compare the photoresponses. Experiments varying the applied potential (E_{app}) were carried out for all the electrodes in both the presence and absence of CH₃OH. In the E_{app} vs photocurrent density plots performed for each electrode, the higher photoactivities were consistently observed for the N-doped In₂O₃ electrodes using methanol as a hole scavenger. With the addition of methanol, the photocurrent density of (am) N-doped In₂O₃ electrodes under visible irradiation is higher than that of (en) N-doped In₂O₃ electrodes. This result is in good agreement with the UV-vis spectra (Figure 6), which demonstrate (am) N-doped In₂O₃ nanoparticles have a smaller band gap energy than (en) N-doped In₂O₃ nanoparticles. The photoelectrochemical experiments were repeated several months later with the finding that the photocurrents were reproducible, indicating that our N-doped In₂O₃ materials are stable over long time periods.

For the TiO₂ electrodes, the photocurrent densities in the presence of methanol increased by a factor of 5, indicating that the charge recombination problem is even more severe than for In₂O₃ without sacrificial reagents. Oxygen photoevolution on the TiO₂ electrode surface produces several reaction intermediates, leading to rapid carrier recombination especially in powered systems without any band bending.^{74,76} Previous work has shown that the peroxo titanium species appear to affect the photochemical behavior of TiO₂ mainly by controlling the e^-/h^+

surface recombination rate.⁷⁶ The surface states of these species act as more effective electron traps than water molecules (or hydronium ions), and as a result, water splitting is a secondary pathway at irradiated TiO₂ particles in the absence of a sacrificial reagent. Presumably similar effects are present at the In₂O₃ surface, although perhaps to a lesser extent due to its better conductivity.

The photoelectrochemical measurements presented in this section show comparative trends of undoped versus doped In₂O₃ materials. However, the photoelectrochemical properties of our electrodes were not optimized according to film thickness or dopant concentration, which could at least partly explain why our photocurrent densities are not higher. Other key factors that decrease the efficiency of powder semiconductor electrodes are the electron/hole lifetime, the random orientation of nanoparticles in the film, and the loss of electron transport originating from the many grain boundaries. Additional studies addressing these factors could be beneficial for the development of more efficient materials.

4. Conclusions

A novel photocatalyst, N-doped In₂O₃, synthesized by simple solvothermal reaction has been found to show enhanced photoelectrochemical activity for water splitting under UV- and visible-light irradiation compared to undoped In₂O₃. N-doped In₂O₃ appears to demonstrate red shifts in absorption and band gap narrowing similar to those of N-doped TiO₂, but with significantly better photoelectrochemical activity for water

splitting. The characterization results, specifically XPS, show that nitrogen has been incorporated into the lattice of In₂O₃ in substitutional and interstitial doping mechanisms depending on the N source used. However, further in-depth experiments are needed to understand completely the structural nature of these nitrogen doping species. Previous work by our research group has shown that NMR has great potential to provide much-needed insights for these dopant species.^{35,69} Additional ¹⁵N NMR experiments are under way to further elucidate the structure of these N-doped In₂O₃ materials. Studies are also being conducted to design thicker electrodes and to investigate the effects of anion dopant concentration on the visible absorption and the photoactivity under visible light. Additional anion doping studies may provide promising avenues for the development of highly efficient photocatalysts for solar hydrogen conversion using large band gap d¹⁰ metal oxides.

Acknowledgment. Financial support by the National Science Foundation (CHE-0616748) and the Purdue Research Foundation is gratefully acknowledged. The authors thank Debby Sherman, Life Science Microscopy Facility Manager at Purdue University, for the acquisition of SEM images. The authors also thank Dr. D. Zemlyanov of the Surface Analysis Laboratory in the Birck Nanotechnology Center/Discovery Park at Purdue University for acquisition of the XPS spectra. D.R. is a member of the Purdue Energy Center at Discovery Park.

Supporting Information Available: IR spectra of undoped commercial In₂O₃, (en) N-doped In₂O₃, and (am) N-doped In₂O₃ powders. This material is available free of charge via the Internet at <http://pubs.acs.org>.

References and Notes

- (1) Fujishima, A.; Honda, K. *Nature* **1972**, 238, 37.
- (2) Santato, C.; Ulmann, M.; Augustynski, J. *J. Phys. Chem. B* **2001**, 105, 936.
- (3) Santato, C.; Ulmann, M.; Augustynski, J. *Adv. Mater.* **2001**, 13, 511.
- (4) Paluselli, D.; Marsen, B.; Miller, E. L.; Rocheleau, R. E. *Electrochem. Solid-State Lett.* **2005**, 8, G301.
- (5) Sartoretti, C. J.; Alexander, B. D.; Solarz, R.; Rutkowska, I. A.; Augustynski, J.; Cerny, R. *J. Phys. Chem. B* **2005**, 109, 13685.
- (6) Duret, A.; Gratzel, M. *J. Phys. Chem. B* **2005**, 109, 17184.
- (7) Klosek, S.; Raftery, D. *J. Phys. Chem. B* **2001**, 105, 2815.
- (8) Di Paola, A.; Marci, G.; Palmisano, L.; Schiavello, M.; Uosaki, K.; Ikeda, S.; Ohtani, B. *J. Phys. Chem. B* **2002**, 106, 637.
- (9) Sene, J. J.; Zeltner, W. A.; Anderson, M. A. *J. Phys. Chem. B* **2003**, 107, 1597.
- (10) Reddy, E. P.; Sun, B.; Smirniotis, P. G. *J. Phys. Chem. B* **2004**, 108, 17198.
- (11) Ghosh, A. K.; Maruska, H. P. *J. Electrochem. Soc.* **1977**, 124, 1516.
- (12) Borgarello, E.; Kiwi, J.; Grätzel, M.; Pelizzetti, E.; Visca, M. *J. Am. Chem. Soc.* **1982**, 104, 2996.
- (13) Tafalla, D.; Salvador, P.; Benito, R. M.; Salvador, P. *J. Electrochem. Soc.* **1990**, 137, 1810.
- (14) Siripala, W.; Ivanovskaya, A.; Jaramillo, T. F.; Baek, S.; McFarland, E. W. *Sol. Energy Mater. Sol. Cells* **2003**, 77, 229.
- (15) Jia, H.; Zhang, Y.; Chen, X.; Shu, J.; Luo, X.; Zhang, Z.; Yu, D. *Appl. Phys. Lett.* **2003**, 82, 4146.
- (16) Khan, S. U. M.; Al-Shahry, M.; Ingler Jr., W. B. *Science* **2002**, 297, 2243.
- (17) Sakthivel, S.; Kisch, H. *Angew. Chem., Int. Ed.* **2003**, 42, 4908.
- (18) Noworyta, K.; Augustynski, J. *Electrochem. Solid-State Lett.* **2004**, 7, E31.
- (19) Luo, H.; Takata, T.; Lee, Y.; Zhao, J.; Domen, K.; Zhao, J.; Yan, Y. *Chem. Mater.* **2004**, 16, 846.
- (20) Neumann, B.; Bogdanoff, P.; Tributsch, H.; Sakthivel, S.; Kisch, H. *J. Phys. Chem. B* **2005**, 109, 16579.
- (21) Park, J. H.; Kim, S.; Bard, A. J. *Nano Lett.* **2006**, 6, 24.
- (22) Barnes, P. R. F.; Randeniya, L. K.; Murphy, A. B.; Gwan, P. B.; Plumb, I. C.; Glasscock, J. A.; Grey, I. E.; Li, C. *Dev. Chem. Eng. Miner. Process.* **2006**, 14, 51.
- (23) Asahi, R.; Morikawa, T.; Ohwaki, T.; Aoki, K.; Taga, Y. *Science* **2001**, 293, 269.
- (24) Irie, H.; Watanabe, Y.; Hashimoto, K. *J. Phys. Chem. B* **2003**, 107, 5483.
- (25) Burda, C.; Lou, Y.; Chen, X.; Samia, A. C. S.; Stout, J.; Gole, J. L. *Nano Lett.* **2003**, 3, 1049.
- (26) Yin, S.; Yamaki, H.; Komatsu, M.; Zhang, Q.; Wang, J.; Tang, Q.; Saito, F.; Sato, T. *J. Mater. Chem.* **2003**, 13, 2996.
- (27) Diwald, O.; Thompson, T. L.; Goralski, E. G.; Walck, S. D.; Yates, J. T. *J. Phys. Chem. B* **2004**, 108, 52.
- (28) Diwald, O.; Thompson, T. L.; Zubkov, T.; Goralski, E. G.; Walck, S. D.; Yates, J. T. *J. Phys. Chem. B* **2004**, 108, 6004.
- (29) Chen, X.; Burda, C. *J. Phys. Chem. B* **2004**, 108, 15446.
- (30) Miyauchi, M.; Ikezawa, A.; Tobimatsu, H.; Irie, H.; Hashimoto, K. *Phys. Chem. Chem. Phys.* **2004**, 6, 865.
- (31) Sano, T.; Negishi, N.; Koike, K.; Takeuchi, K.; Matsuzawa, S. *J. Mater. Chem.* **2004**, 14, 380.
- (32) Aita, Y.; Komatsu, M.; Yin, S.; Sato, T. *J. Solid State Chem.* **2004**, 177, 3235.
- (33) Sato, S. *Chem. Phys. Lett.* **1986**, 123, 126.
- (34) Sakatani, Y.; Nunoshige, J.; Ando, H.; Okusako, K.; Koike, H.; Takata, T.; Kondo, J. N.; Hara, M.; Domen, K. *Chem. Lett.* **2003**, 32, 1156.
- (35) Reyes-Garcia, E. A.; Sun, Y.; Reyes-Gil, K.; Raftery, D. *J. Phys. Chem. C* **2007**, 111, 2738.
- (36) Di Valentin, C.; Pacchioni, G.; Selloni, A.; Livraghi, S.; Giamello, E. *J. Phys. Chem. B* **2005**, 109, 11414.
- (37) Nakamura, R.; Tanaka, T.; Nakato, Y. *J. Phys. Chem. B* **2005**, 109, 8920.
- (38) Murase, T.; Irie, H.; Hashimoto, K. *J. Phys. Chem. B* **2004**, 108, 15803.
- (39) Inoue, Y. *Chem. Ind.* **2006**, 108, 623.
- (40) Hwang, D. W.; Kim, H. G.; Lee, J. S.; Kim, J.; Li, W.; Oh, S. H. *J. Phys. Chem. B* **2005**, 109, 2093.
- (41) Abe, R.; Higashi, M.; Sayama, K.; Abe, Y.; Sugihara, H. *J. Phys. Chem. B* **2006**, 110, 2219.
- (42) Abe, R.; Higashi, M.; Zou, Z.; Sayama, K.; Abe, Y.; Arakawa, H. *J. Phys. Chem. B* **2004**, 108, 811.
- (43) Kudo, A.; Kato, H.; Nakagawa, S. *J. Phys. Chem. B* **2000**, 104, 571.
- (44) Sato, J.; Saito, N.; Nishiyama, H.; Inoue, Y. *J. Phys. Chem. B* **2001**, 105, 6061.
- (45) Sato, J.; Saito, N.; Nishiyama, H.; Inoue, Y. *J. Phys. Chem. B* **2003**, 107, 7965.
- (46) Nozik, A. J. *Annu. Rev. Phys. Chem.* **1978**, 29, 189.
- (47) Li, Z.; Dong, T.; Zhang, Y.; Wu, L.; Li, J.; Wang, X.; Fu, X. *J. Phys. Chem. C* **2007**, 111, 4727.
- (48) Kudo, A.; Mikami, I. *Chem. Lett.* **1998**, 1027.
- (49) Poznyak, S. K.; Talapin, D. V.; Kulak, A. I. *J. Phys. Chem. B* **2001**, 105, 4816.
- (50) Hara, K.; Sayama, K.; Arakawa, H. *Sol. Energy Mater. Sol. Cells* **2000**, 62, 441.
- (51) Wang, D.; Zou, Z.; Ye, J. *Chem. Mater.* **2005**, 17, 3255.
- (52) Xu, Y.; Schoonen, M. A. A. *Am. Mineral.* **2000**, 85, 543.
- (53) Yu, D.; Yu, W.; Wang, D.; Qian, Y. *Thin Solid Films* **2002**, 419, 166.
- (54) Reyes-Gil, K.; Reyes-Garcia, E.; Raftery, D. *J. Electrochem. Soc.* **2006**, 153, A1296.
- (55) Grätzel, M. *J. Sol-Gel Sci. Technol.* **2001**, 22, 7.
- (56) Fairley, N.; Carrick, A. *The Casa Cookbook, Part I: Recipes for XPS Data Processing*; Acolyte Science: Knutsford, 2005.
- (57) Sakthivel, S.; Janczarek, M.; Kisch, H. *J. Phys. Chem. B* **2004**, 108, 19384.
- (58) Willson, R. C. *Sol. Phys. (Hist. Arch.)* **1981**, 74, 217.
- (59) Gole, J. L.; Stout, J. D.; Burda, C.; Lou, Y.; Chen, X. *J. Phys. Chem. B* **2004**, 108, 1230.
- (60) Yates, H. M.; Nolan, M. G.; Sheel, D. W.; Pemble, M. E. *J. Photochem. Photobiol., A* **2006**, 179, 213.
- (61) Gurlo, A.; Ivanovskaya, M.; Barsan, N.; Weimar, U. *Inorg. Chem. Commun.* **2003**, 6, 569.
- (62) Sorescu, M.; Diamandescu, L.; Tarabasanu-Mihaila, D.; Teodorescu, V. S. *J. Mater. Sci.* **2004**, 39, 675.
- (63) Okato, T.; Sakano, T.; Obara, M. *Phys. Rev. B* **2005**, 72, 115124.
- (64) Donley, C.; Dunphy, D.; Paine, D.; Carter, C.; Nebesny, K.; Lee, P.; Alloway, D.; Armstrong, N. R. *Langmuir* **2002**, 18, 450.
- (65) Maruyama, T.; Yoroze, K.; Noguchi, T.; Seki, Y.; Saito, Y.; Araki, T.; Nanishi, Y. *Phys. Status Solidi C* **2003**, 0, 2031.
- (66) Lee, I. J.; Kim, J.-Y.; Shin, H.-J. *J. Appl. Phys.* **2004**, 95, 5540.
- (67) Sathish, M.; Viswanathan, B.; Viswanath, R. P.; Gopinath, C. S. *Chem. Mater.* **2005**, 17, 6349.
- (68) Asai, N.; Inoue, Y.; Sugimura, H.; Takai, O. *J. Electrochem. Soc.* **1999**, 146, 2365.

- (69) Reyes-Garcia, E.; Sun, Y.; Raftery, D. *J. Phys. Chem. C*, accepted, 2007.
- (70) Sato, S.; Nakamura, R.; Abe, S. *Appl. Catal., A* **2005**, 284, 131.
- (71) Rodriguez, J. A.; Jirsak, T.; Dvorak, J.; Sambasivan, S.; Fischer, D. *J. Phys. Chem. B* **2000**, 104, 319.
- (72) Burda, C.; Gole, J. *J. Phys. Chem. B* **2006**, 110, 7081.
- (73) Gopinath, C. S. *J. Phys. Chem. B* **2006**, 110, 7079.
- (74) Thompson, T. L.; Yates, J. T., Jr. *J. Phys. Chem. B* **2005**, 109, 18230.
- (75) Wahl, A.; Ulmann, M.; Carroy, A.; Jermann, B.; Dolata, M.; Kedzierzawski, P.; Chatelain, C.; Monnier, A.; Augustynski, J. *J. Electroanal. Chem.* **1995**, 396, 41.
- (76) Ulmann, M.; de Tacconi, N. R.; Augustynski, J. *J. Phys. Chem.* **1986**, 90, 6523.
- (77) Farfan-Arribas, E.; Madix, R. J. *J. Phys. Chem. B* **2003**, 107, 3225.
- (78) Chen, X.; Lou, Y.; Samia, A. C. S.; Burda, C.; Gole, J. L. *Adv. Funct. Mater.* **2005**, 15, 41.